THE JOURNAL OF PHYSICAL CHEMISTRY C
A JOURNAL OF THE AMERICAN CHEMICAL SOCIETY

pubs.acs.org/JPCC

Article

Unlocking Water Adsorption Mechanisms in Y-BTC MOF: Insights from XAFS and SSNMR Spectroscopy

Jiabin Xu, Jingsong Wang, Xinyue Sheng, Hui Ding, Jun Xu, Shoushun Chen, Ivan Hung, Zhehong Gan, Youyong Li, Jun Zhong,* Tsun-Kong Sham,* and Yining Huang*

Cite This: J. Phys. Chem. C 2025, 129, 17341−17352

Read Online

ACCESS | Metrics & More | Article Recommendations | Supporting Information

ABSTRACT: Water plays a critical role in natural and technological processes, including atmospheric water harvesting, electrocatalysis, and biochemical reactions, all of which involve interactions between water and materials. Metal−organic frameworks (MOFs), with their tunable porosity and adsorption sites, offer significant potential in these fields. Understanding the interactions of water with MOFs is essential for optimizing their performance. This study investigates water adsorption behavior and dynamics in a yttrium-based MOF (Y-BTC) with open metal sites using X-ray absorption fine structure (XAFS) spectroscopy, solid-state nuclear magnetic resonance (SSNMR), and Monte Carlo (MC) simulations. XAFS reveals local structural changes upon coordinated water removal, producing open metal sites, while SSNMR provides insights into water mobility and adsorption site preferences under varying relative humidity (RH) conditions. MC simulations further validate these findings by mapping the water distribution within the framework. The results highlight that water adsorption in Y-BTC involves multiple adsorption sites and dynamic rearrangements, with the framework itself undergoing subtle structural evolution at lower temperatures. These findings enhance our understanding of water adsorption mechanisms in MOFs and offer valuable insights for the rational design of materials for water harvesting.

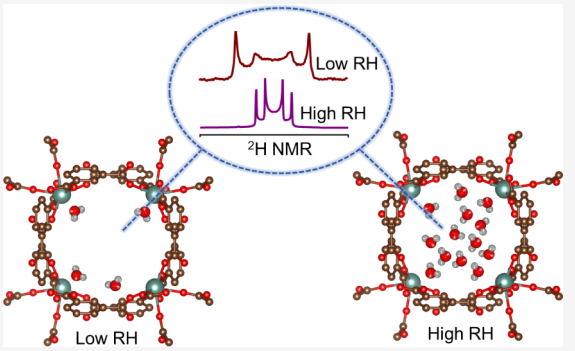

INTRODUCTION

Water is essential and ubiquitous in nature, participating in biological, chemical, and geological processes. Its interactions with materials are crucial in various technologies, including atmospheric water harvesting,[1−3] high-temperature cooling,[4] heterogeneous catalysis,[5,6] electrochemical water splitting,[7,8] and water-assisted reactions.[9−11] In these applications, water adsorption, storage, and transport at the molecular level directly impact performance, making it essential to develop a detailed understanding of interactions between water and materials for material design and optimization.

Benefiting from well-defined structures and tunable chemical and geometric properties, metal−organic frameworks (MOFs) are promising materials for water-related applications. Their ability to selectively adsorb and regulate water within the pores makes them attractive for energy-efficient water capture, catalytic transformations, and electrochemical processes.[7,12,13] However, despite extensive studies, the fundamental mechanisms of water adsorption and dynamics within MOFs remain insufficiently understood, limiting their rational design for practical applications.

A key challenge is identifying specific adsorption sites and understanding how water molecules interact within MOFs. Manipulating the strength of adsorption sites is crucial for optimizing MOFs in various applications, whether enhancing water uptake capacity or facilitating rapid desorption. In particular, MOFs with open metal sites often exhibit enhanced guest adsorption due to the strong interaction between water molecules and open metal sites.[14,15] These open metal sites are created by the removal of coordinated solvent molecules at the metal sites during activation, typically achieved by heating under vacuum.[16] Moreover, water confined within nanoscopic environments exhibits unique behaviors distinct from its bulk liquid state.[17] A deeper understanding of water in confinement not only benefits materials science but may also provide insights into biological functions.[18,19]

Rare-earth MOFs are particularly intriguing due to their high metal coordination numbers, which improve their water stability, and their diverse coordination environments, which enable intricate topologies dictated primarily by ligand steric effects.[20,21] Among rare-earth MOFs, one yttrium-based MOF, $Y(BTC)(H_2O)\bullet xH_2O\bullet yDMF$ (Y-BTC, BTC = 1,3,5-benzenetricarboxylate, DMF = N,N-dimethylformamide), also

Received: August 2, 2025
Revised: September 8, 2025
Accepted: September 10, 2025
Published: September 15, 2025

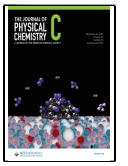

https://doi.org/10.1021/acs.jpcc.5c05403
J. Phys. Chem. C 2025, 129, 17341−17352

known as MOF-76, presents an ideal system for studying interactions with water molecules.[16,22−24] Its flexible framework contains a coordinated water molecule at each Y^{3+} site that can be removed to generate open metal sites. Note that as early as 2008, Luo et al. reported that Y-BTC is an unusual MOF with open metal sites, where the strongest adsorption sites for hydrogen (D_2) are the aromatic BTC linker instead of the open metal sites.[24] Generally, open metal sites strongly interact with guest molecules, which is a key design feature of MOFs.[25−27] Moreover, Ogilvie et al. similarly found that guest molecules like deuterated methane and molecular oxygen interact primarily with the bridging ligands rather than directly with Y^{3+} sites, although multiple adsorption sites are present.[28] The authors further reported that both CD_4 and CO_2 cannot directly interact with Y^{3+} sites, as access to Y^{3+} is sterically hindered by structural rearrangements upon removal of coordinated water, i.e., the reconfiguration of O−Y−O bond angles encloses the open metal sites.[16] However, they found O_2 is able to reopen the O−Y−O angles, restoring access to Y^{3+}, which shows the structural change induced by guest interaction.[16,28] A similar phenomenon is prevalent in flexible MOFs.[29−31] As reported in our previous study,[29] a sharp increase in adsorption isotherms indicates structural opening.

Herein, we present a comprehensive study on water adsorption mechanisms in the Y-BTC MOF. First, the local structure of Y ions in Y-BTC is revealed by XAFS, suggesting a structural transformation upon removal of coordinated water, producing open metal sites that may influence adsorption behavior. To probe water adsorption behavior under varying conditions, we employ ^{2}H SSNMR experiments on samples equilibrated at different relative humidity (RH) levels, uncovering multiple adsorption sites and dynamics changes across a broad temperature range. Monte Carlo (MC) simulations further support the idea that open metal sites serve as one of the adsorption sites. This means that water, like O_2, is also able to induce exposure of Y^{3+} sites. ^{1}H−^{13}C CP-MAS and ^{1}H MAS results reveal subtle local structural changes of the BTC linkers induced by the presence of water upon cooling. VT ^{2}H SSNMR experiments demonstrate that water molecules form clusters at temperatures below −40 °C and undergo redistribution after heating: water molecules initially bind to the open metal sites, followed by adsorption at other sites with higher water mobility as the temperature increases.

EXPERIMENTAL METHODS

Materials. All substances were used as received, without further purification: yttrium(III) nitrate hexahydrate ($Y(NO_3)_3{\cdot}6H_2O$, 99.8%, Sigma-Aldrich), benzene-1,3,5-tricarboxylic acid (BTC, $C_9H_6O_6$, 95%, Sigma-Aldrich), potassium sulfate (K_2SO_4, 99%, Thermo Scientific Chemicals), magnesium nitrate hexahydrate ($Mg(NO_3)_2{\cdot}6H_2O$, 99%, Sigma-Aldrich), magnesium chloride ($MgCl_2$, 98%, Sigma-Aldrich), potassium acetate (CH_3COOK, 99%, Sigma-Aldrich), lithium chloride (LiCl, 99%, Sigma-Aldrich), potassium hydroxide (KOH, 85%, Sigma-Aldrich), ethanol (99%, Fischer Chemicals), and deuterium oxide (D_2O, 99.9%, Sigma-Aldrich).

Synthesis. Y-BTC was synthesized according to the reported procedure with minor modifications.[22] Briefly, a mixture of $Y(NO_3)_3{\cdot}6H_2O$ (1.5 mmol) and BTC (0.75 mmol) was dissolved in 12 mL of DMF and 12 mL of H_2O at room temperature. The mixture was transferred to a 50 mL Teflon autoclave, sealed, and heated in an oven at 100 °C for 24 h. After vacuum filtration, the resulting white needle-like powder was dried in an oven at 80 °C overnight, then ground into a fine powder, denoted as Y-BTC-asmade. The powder was then activated under vacuum at 200 °C for 12 h, named as Y-BTC-act.

Water Loading. Y-BTC-act was loaded into an open small vial and placed in a sealed container containing a saturated salt solution at room temperature. The relative humidity (RH) was controlled by using different saturated salt solutions. The RH values for the saturated solutions of K_2SO_4, $Mg(NO_3)_2$, $MgCl_2$, CH_3COOK, LiCl, and KOH solution were approximately 97%, 53%, 33%, 23%, 11%, and 8%, respectively. After 1 week, once adsorption equilibrium was reached, the samples were ready for SSNMR experiments.

Powder X-ray Diffraction. Powder X-ray diffractograms were recorded on a Rigaku powder diffractometer using Cu Kα radiation (λ = 1.5406 Å). Reflections were collected at 2θ values ranging from 5° to 45°. In situ synchrotron-based powder XRD patterns were collected with wavelengths of 0.2095 Å at the High Energy Wiggler Beamline of the Brockhouse Diffraction Sector (BXDS-WHE) in the Canadian Light Source (CLS). The sample was loaded into Kapton capillaries with a diameter of 0.8 mm and sealed with epoxy glue. The sample was first cooled down to −120 °C and then measured every 30° until the temperature reached 230 °C.

Water Vapor Adsorption Measurements. Water vapor adsorption isotherm measurements were carried out on a BELSORP-MAX instrument at 298 K. Prior to H_2O isotherm measurements, the samples were activated by degassing via dynamic vacuum and heating for 10 h at 200 °C.

Solid-State NMR. ^{2}H static SSNMR experiments were performed on a Varian Infinity Plus NMR spectrometer at a magnetic field of 9.4 T ($\nu_0(^2H)$ = 61.42 MHz) using a Varian/Chemagnetics 5 mm HX static probe. ^{2}H chemical shifts were referenced to D_2O at −4.62 ppm. The spectra were collected using the quadrupolar echo sequence[32] with an optimized ^{2}H 90° pulse length of 3.6 μs and recycle delay of 1 s. Analytical simulations of ^{2}H experimental spectra to extract the parameters (C_Q and η_Q) were performed using the dmfit software.[33]

^{1}H−^{13}C CP-MAS NMR experiments were performed with a Varian/Chemagnetics 5 mm HFXY MAS probe at a spinning rate of 8 kHz. The contact time was 3 ms, a ^{1}H 90° pulse length of 5.4 μs, and a recycle delay of 5 s were used. The Hartmann−Hahn matching condition was set up using solid adamantane. ^{13}C chemical shifts were referenced to tetramethylsilane (TMS), using methylene carbon in ethanol as a secondary reference at 58.05 ppm. Corresponding ^{1}H MAS NMR spectra were also collected at the same time, and ^{1}H chemical shifts were referenced to tetramethylsilane (TMS) by using the CH_2 chemical shift of solid adamantane as a secondary reference at 1.85 ppm. All experimental temperatures were measured with an uncertainty of ± 2 K using a Varian variable temperature (VT) control unit.

^{1}H−^{89}Y CP-MAS NMR experiments were performed using a 4 mm low-γ HX MAS probe on a Bruker Avance III spectrometer at a magnetic field strength of 14.1 T ($\nu_0(^{89}Y)$ = 29.4 MHz) in Beijing, China, and a 3.2 mm low-γ HXY MAS probe on a Bruker Avance III spectrometer at a magnetic field strength of 18.8 T ($\nu_0(^{89}Y)$ = 39.2 MHz) at the National High Magnetic Field Laboratory (NHMFL), Florida, USA. At 18.8 T, the spinning rate was 10 kHz. A recycle delay of 3.2 s and a contact time of 20.0 ms were used. At 14.1 T, the spinning rate was 5 kHz, and a recycle delay of 5.0 s was used. The

https://doi.org/10.1021/acs.jpcc.5c05403
J. Phys. Chem. C 2025, 129, 17341−17352

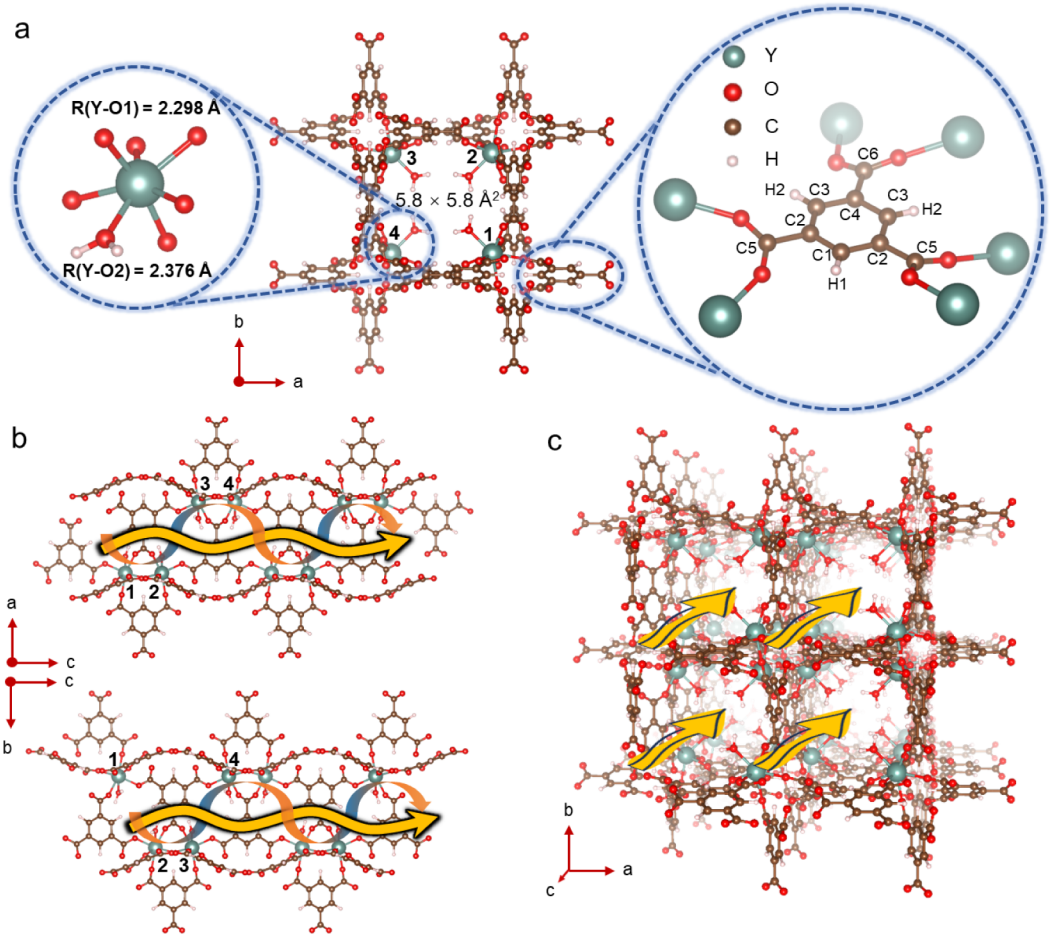

Figure 1. Schematic illustration of the crystal structure of Y-BTC (a) from an *a* and *b*-axis view, (b) from *a*, *c*-axis and *b*, *c*-axis view, and (c) from a perspective view. The orange-blueish curve with arrows represents the arrangement of Y, showing a helical chain progression along the 1D channel from one side to the other. The yellow curve with arrows shows a zigzag 1D channel that allows water molecules to pass through. The pore size of the 1D channel is 5.8 × 5.8 Å. The enlarged view on the left shows that the central Y atom is coordinated by six oxygen atoms from the ligands and one from the water molecule. The enlarged view on the right hghlights six inequivalent carbon environments within the BTC ligand.

Hartmann−Hahn matching conditions for $^{1}H-^{89}Y$ CP-MAS NMR experiments were optimized using $Y(OH)_3$, with a ^{1}H 90° pulse of 3 μs and a contact time of 8.0 ms. ^{89}Y chemical shift was also referenced to $Y(OH)_3$ as 68 ppm.[34]

XAS Experiments. In-situ XAFS experiments at Y K-edges were performed at the Hard X-ray Micro-Analysis beamline (HXMA) of the Canadian Light Source (CLS) in Saskatoon, SK. Powder samples were pressed into pellets and mounted on the sample holder. The in situ heating cell is equipped with circulating water equipment to maintain the designated temperature. All the Y spectra were collected in transmission mode and analyzed using Athena.[35] The EXAFS data were fitted using Artemis.[35] In-situ O K-edge XANES spectra were acquired at the Spherical Grating Monochromator beamline (SGM) of CLS. Powder samples were also pressed into thin pellets and mounted on the sample holder. After evacuating the sample chamber, the holder was heated from room temperature to 120 °C. Before acquiring data at each selected temperature, the system was allowed to stabilize for 15 min. The spectra were recorded in fluorescence mode.

Computational Details. To investigate the adsorption mechanism of H_2O in Y-BTC, we employed computational simulations, specifically Monte Carlo (MC) simulations,[36] using the Sorption module in Materials Studio. The adsorption of H_2O onto Y-BTC was studied within a 2 × 2 × 2 supercell of the framework. Van der Waals interactions between the adsorbates and adsorbents were modeled using the universal force field,[37,38] with a cutoff distance of 8.5 Å. To ensure the reliability of the simulations, 1.0×10^6 equilibration steps were performed at 298 K. Subsequently, 1.0×10^7 production steps were carried out to generate an ensemble of configurations representing both the adsorbates and adsorbents. Partial charges for both the adsorbates and adsorbents were calculated using the QEq method,[39] while electrostatic interactions were computed using the Ewald summation technique.[40] Both the adsorbates and adsorbents were treated as electrically neutral, with hydrogen bonding being the primary interaction between H_2O and the framework.

RESULTS AND DISCUSSION

Y-BTC MOF was prepared via the solvothermal method using H_2O and DMF as solvents, according to the literature.[22] In its crystal structure, each yttrium (Y) atom is coordinated by seven oxygen atoms, including six from six individual benzene-1,3,5-tricarboxylic acid (BTC) linkers and one from a coordinated water molecule, and each BTC linker connects with six Y atoms (Figure 1a). The Y−O bond distances, therefore, exhibit two distinct values due to the different oxygen environments. The bond length between Y and the

https://doi.org/10.1021/acs.jpcc.5c05403
J. Phys. Chem. C 2025, 129, 17341−17352

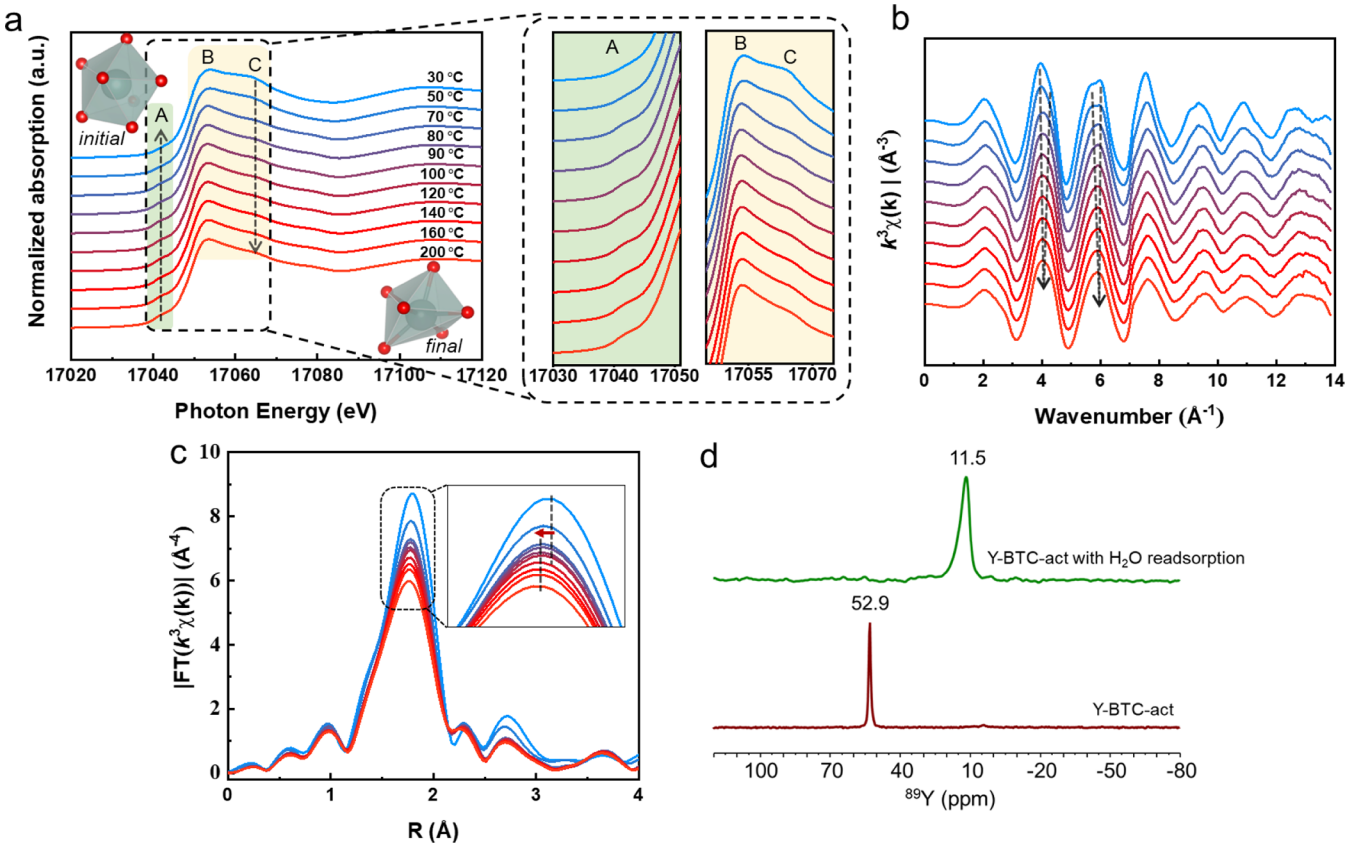

Figure 2. (a) In-situ Y K-edge XANES spectra of Y-BTC as a function of temperature from 30 to 200 °C. The inset shows the local coordination environment of central Y atoms at the initial (seven-coordinated by O atoms) and final states (six-coordinated by O atoms). Red: oxygen; gray: yttrium. (b) The corresponding k^3-weighted EXAFS spectra in k space. (c) The corresponding Fourier-transformed EXAFS spectra in R space. The inset shows the peak left-shifts to a smaller distance upon heating. (d) ^{1}H−^{89}Y CP-MAS SSNMR spectra of Y-BTC-act and Y-BTC-act after the readsorption of water. The spinning rate is 10 kHz. A contact time of 20 ms and a recycle delay of 3.2 s were used for data acquisition.

oxygen from the coordinated water molecule is 2.376 Å, slightly longer than the Y−O bonds from the BTC linkers (2.298 Å). From the view of the *a* and *b* axis, Y-BTC features a tetragonal porous framework (space group: $P4_322$) with a one-dimensional (1D) channel of 5.8 × 5.8 Å^2 along the *c* axis (Figure 1a,c).[24] Interestingly, the Y atoms, instead of staying at the same plane, present a helical chain progression along the 1D channel,[16,22] as presented in Figure 1b. Consequently, water molecules inside the MOF pore channels follow a zigzag distribution pattern (yellow arrows in Figure 1).

The XRD pattern of the as-synthesized Y-BTC (denoted as Y-BTC-asmade) matches well with the calculated pattern from the crystal structure (Figure S1a), confirming the successful synthesis. The coordinated water molecule can be removed through heat treatment under vacuum, leaving Y in a six-coordinated environment. TGA results prove that adsorbed water is fully removed at 100 °C, while residual DMF in the pores is eliminated at 200 °C (Figure S2). Therefore, the activation of Y-BTC is conducted at 200 °C, and the resulting powder is referred to as Y-BTC-act hereafter. XRD results confirm that the overall topology of Y-BTC-act remains intact. In situ variable-temperature synchrotron XRD (Figure S1b) further shows structural stability across a wide temperature range (−120−230 °C), as all patterns are very similar. However, slight deviations such as peak splitting and shifts (e.g., 9°, 20°, and 36°) from the 30 °C pattern at both higher and lower temperatures suggest subtle structural evolution that has an impact on water behavior (*vide infra*). In addition, a sharp increase in the water vapor adsorption isotherms (Figure S3), consistent with previous reports,[16] may indicate the structural opening induced by water-framework interactions.

Evolution of the Local Environment around Yttrium. XAFS experiment at the Y K-edge is performed to reveal the possible local structural changes upon the removal of coordinated water. The comparison of the Y K-edge XANES spectra of Y-BTC-asmade at various temperatures is shown in Figure 2a-c. While the overall spectra remain similar, significant differences emerge with increasing temperature. All spectra can be characterized by a whiteline peak B and a shoulder peak C, at about 17053 and 17065 eV, respectively, along with a small pre-edge peak A at 17042 eV. As temperature increases, peak B remains intact, whereas the pre-edge peak A becomes more intense, and peak C becomes barely discernible. At the initial temperature of 30 °C, the center Y atom is coordinated by seven oxygen atoms (including one from coordinated water), adopting an irregular decahedral geometry (schematic model in Figure 2a). Upon heating, the coordinated water is removed, and the Y coordination environment transitions into an irregular octahedron. The enhanced intensity of pre-edge peak A infers increased distortion in this six-coordinated geometry compared to the original seven-coordinated configuration.[41] The gradually decreased intensity of peak C may also be attributed to the loss of the longer Y−O bond associated with the coordinated water, leaving only the shorter Y−O bonds from the BTC linkers. To validate the change in the oxygen environment, in situ O K-edge XANES experiments

https://doi.org/10.1021/acs.jpcc.5c05403
J. Phys. Chem. C 2025, 129, 17341−17352

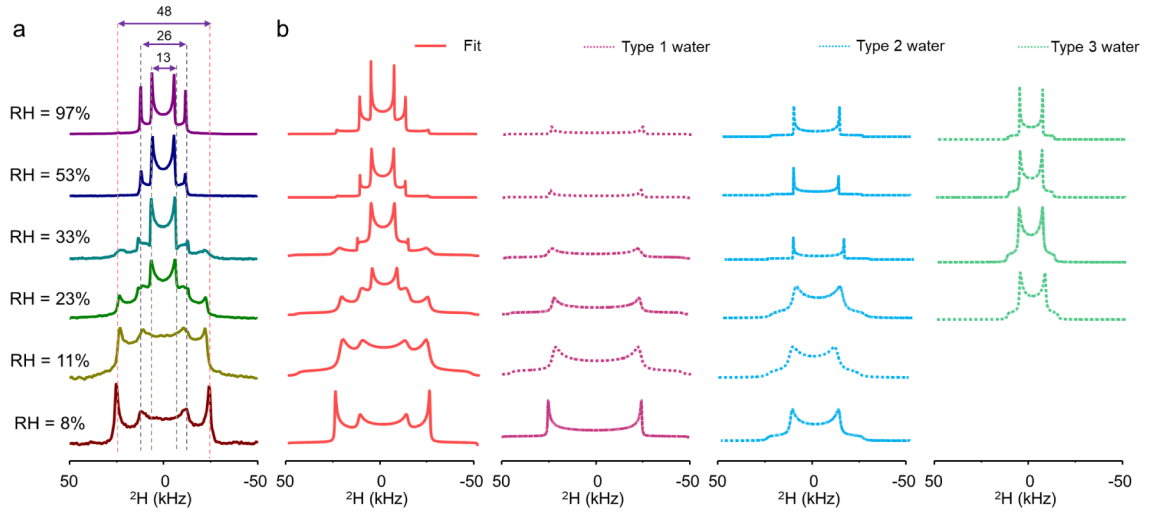

Figure 3. (a) Experimental and (b) simulated ^{2}H static SSNMR spectra of D_2O adsorbed in Y-BTC at different relative humidity (RH) environments at room temperature. Note that the number indicates the line width of doublets in kHz.

were conducted to observe the corresponding changes from the oxygen perspective (Figure S4). Unfortunately, across the temperature range from room temperature to 120 °C, no significant differences were observed . This is likely because most of the oxygen content originates from the BTC linkers, and after averaging, the subtle changes become indistinguishable.

The validity of the aforementioned inference is further confirmed by a comparison of the EXAFS spectra. As shown in Figure 2b, the k^3-weighted EXAFS spectra at Y K-edges present merging peaks in the low k region (3−7 $Å^{-1}$) as the temperature increases. In this region, the amplitude is mainly influenced by interference between the central Y atom and its neighboring light atoms, i.e., oxygen.[42] Therefore, the observed peak splits in the low k region correspond to Y−O scattering paths with different interatomic distances, as mentioned above. After removal of the coordinated water molecules, one of the Y−O paths vanishes, leaving only the remaining shorter Y−O bonds.

A deeper understanding of the local environment around Y atoms is obtained through quantitative EXAFS analysis. The Fourier transform (FT) of the EXAFS region (without phase correction) reveals a major peak at 1.8 Å, attributed to Y−O scattering, which shows a reduction in the peak amplitude and a slight left-shift to a smaller R value (Figure 2c). EXAFS fitting, performed at the initial temperature of 30 °C and the final temperature of 200 °C for simplicity, provides specific coordination parameters (Figure S5 and Table S1). Initially, the coordination numbers of two types of O from the BTC linker (Y−O1) and coordinated water (Y−O2) are 5.9 and 1.0, respectively. Upon removal of water, only one Y−O1 remained with a coordination number of 6.1. In addition, the removal of the longer Y−O2 bond (2.38 Å) leads to a left-shift of the main peak, which is Y−O1 with a shorter bond distance of 2.28 Å.

For a complement and cross-validation of XAFS results,^{89}Y SSNMR experiments were conducted to characterize the local coordination environment of Y atoms.[43−46] ^{89}Y is a spin-1/2 nucleus; although being 100% naturally abundant, its gyromagnetic ratio (γ) is very low (also known as a low-γ nucleus), rendering low sensitivity and signal-to-noise (S/N) ratio. In addition, it is well-known that the spin−lattice relaxation times (T_1) of ^{89}Y are very long. Therefore, ^{89}Y direct excitation experiments require extremely long recycle delays between scans, sometimes extending to several hours, making it time-consuming to acquire high-quality data.[47,48] To overcome this limitation, cross-polarization (CP) magic angle spinning (MAS) experiments offer a practical and efficient solution by transferring polarization from ^{1}H to ^{89}Y nuclei via heteronuclear dipolar interactions.[44,49] The intrinsic signal sensitivity difference between ^{1}H and ^{89}Y contributes to the superiority of the CP experiments. Moreover, since ^{1}H typically exhibits a much shorter T_1, the recycle delay in ^{1}H−^{89}Y CP-MAS experiments is significantly reduced, enabling faster data acquisition while providing valuable insights into the local environment of Y. As shown in Figure 2d, Y-BTC-act exhibits a more downfield chemical shift of 52.9 ppm compared to Y-BTC-act after water readsorption, which shifts to 11.5 ppm. This trend aligns with XAFS results, confirming that Y-BTC-act adopts a six-coordinate structure, whereas it transitions to a seven-coordinate environment upon water coordination. This chemical shift trend is consistent with reports on Y-based materials with different coordination numbers, where a lower coordination number exhibits a more deshielded resonance.[43,50] Specifically, the removal of coordinated water in a $Y(OH)_8(H_2O)$ environment results in a downfield shift of the ^{89}Y signal from 29.6 to 107.3 ppm in the corresponding $Y(OH)_8$ environment.[51]

Water Adsorption Positions at Different RH Values. To study the water behavior inside the pores, ^{2}H SSNMR experiments were conducted. The sample preparation followed a controlled procedure: Y-BTC was first activated at 200 °C under vacuum overnight. The activated sample, loaded into a glass tube, was then placed inside a sealed container with different saturated salt solutions (using D_2O as the solvent) to maintain specific relative humidity (RH) values (e.g., a saturated $MgCl_2$ solution provides RH = 33% at room temperature).[52] Importantly, the samples were not in direct contact with liquid water. To ensure that water adsorption equilibrium was reached, each sample was allowed to sit for 1 week before NMR data acquisition.

As shown in Figure 3a,^{2}H static NMR experiments were performed on Y-BTC at varying RH levels (8%, 11%, 23%, 33%, 53%, and 97%) to investigate the effect of RH on water adsorption behavior inside the MOF. Apparently, the spectral

https://doi.org/10.1021/acs.jpcc.5c05403
J. Phys. Chem. C 2025, 129, 17341−17352

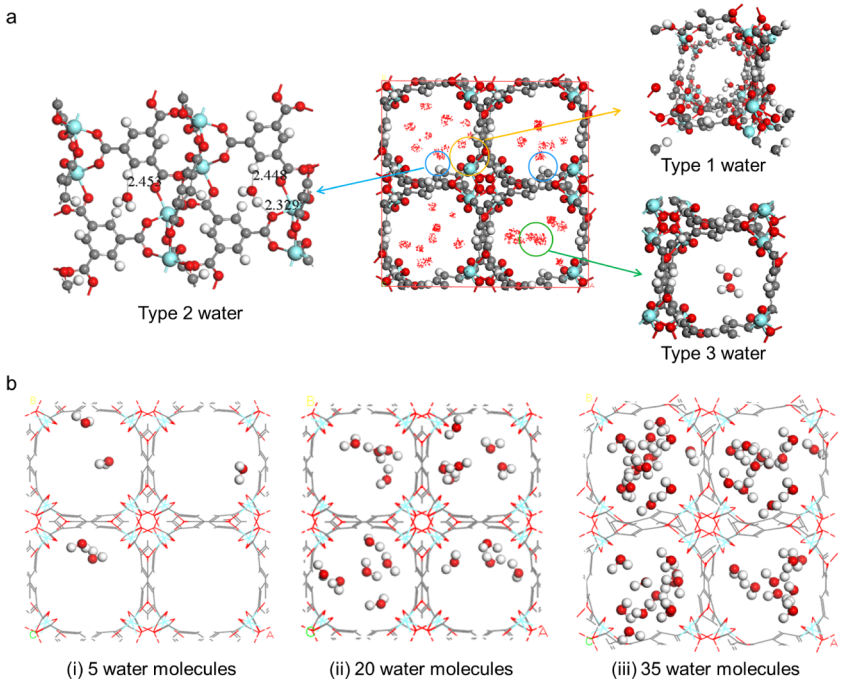

Figure 4. (a) Probability density map of H_2O molecule adsorption in Y-BTC (2 × 2 × 2 supercell), showing three different positions: at metal sites (Type 1 water), through hydrogen-bond bonding with O atoms of BTC linkers (Type 2 water), and at the center of pore channels with hydrogen bonding (Type 3 water). (b) MC-simulated H_2O adsorption in Y-BTC at different loadings: (i) 5 molecules, (ii) 20 molecules, and (iii) 35 molecules per 2 × 2 × 2 supercell.

line shapes exhibit significant RH dependence, with broad line shapes at low RH values and narrow line shapes at high RH values. Spectroscopic parameters such as the quadrupole coupling constant (C_Q) and asymmetry parameter (η) are determined from spectral simulation using the dmfit software,[33] and the derived values are listed in Table S2. Notably, all signals have an asymmetry parameter of η = 0, indicating that the local electric field gradient (EFG) around the nucleus is axially symmetric.[53,54]

At the lowest RH of 8%, the ^{2}H spectrum exhibits two Pake doublets. The first, a broad line shape with C_Q = 67.0 kHz (denoted as Type 1 water), can be assigned to water molecules tightly coordinated to open metal sites (Y^{3+}), where strong interactions result in restricted molecular motion. The second, a weaker and narrower line shape with C_Q = 34.0 kHz (denoted as Type 2 water), likely corresponds to water adsorbed near BTC linkers (*vide infra*), experiencing weaker interactions and thus greater mobility. Upon increasing RH to 23%, a third Pake doublet (C_Q = 18.0 kHz) with higher intensity and lower C_Q appears (denoted as Type 3 water). This signal is indicative of the most mobile water species, which are associated with water molecules engaged in weak hydrogen bonding within the pore channels.[55]

These three distinct spectral features suggest a humidity-dependent, multiposition adsorption mechanism: water is strongly bound at open metal sites (Type 1) at low RH levels, followed by adsorption at linker-associated sites (Type 2) and accumulation in the pore centers with the largest mobility (Type 3) at high RH levels. Supporting this interpretation, the water vapor isotherm (Figure S3) shows that even at RH = 8%, the water uptake reaches approximately 3 mol H_2O per mole Y, well above the 1:1 stoichiometry required for full coordination at Y^{3+} sites. Thus, if water molecules indeed occupy each Y^{3+} site individually, then open metal sites are already saturated at the lowest RH level, and additional water molecules are progressively accommodated at other positions with weaker interactions as RH increases. This explains the growing dominance of Type 2 and Type 3 water signals from RH = 23% onward, while the Type 1 water becomes barely visible at higher RH levels.

To further validate the spatial distribution of adsorbed water, Monte Carlo (MC) simulations were employed (Figure 4). The results clearly identify three distinct adsorption positions that align well with our findings (Figure 4a): Type 1 water is located at the open metal sites, as expected; Type 2 water is positioned close to the BTC ligands, where hydrogen bonding occurs with carboxylate oxygen atoms; and Type 3 water is distributed at the center of pore channels, where water molecules interact with each other via hydrogen bonding. In addition, simulations (Figure 4b) also reveal that at low water loading, water molecules are primarily distributed at the open metal sites and near BTC linkers, whereas at higher loadings, the majority of water molecules occupy the pore centers, forming hydrogen-bonded clusters.

Water Dynamics Study by VT ^{2}H SSNMR. Variable temperature (VT) static ^{2}H NMR experiments were conducted to reveal the dynamics of water molecules inside the MOF (Figure 5). Across all RH conditions, the line shape becomes broader and more featureless as the temperature decreases, suggesting a significant slowdown in the motion rates relative to the time scale of the NMR experiment. Specifically, at RH = 97%, two types of water molecules (Type 2 and Type 3) experience fast motion above −20 °C. However, from −30 to −60 °C, these two distinct lines merge and evolve into a single Lorentzian profile, with a full width at half-height (FWHH) of ∼10 kHz at −50 °C and 13 kHz at −60 °C. This merging likely arises from these two types of weakly adsorbed D_2O species detaching from their original adsorption positions and

https://doi.org/10.1021/acs.jpcc.5c05403
J. Phys. Chem. C 2025, 129, 17341−17352

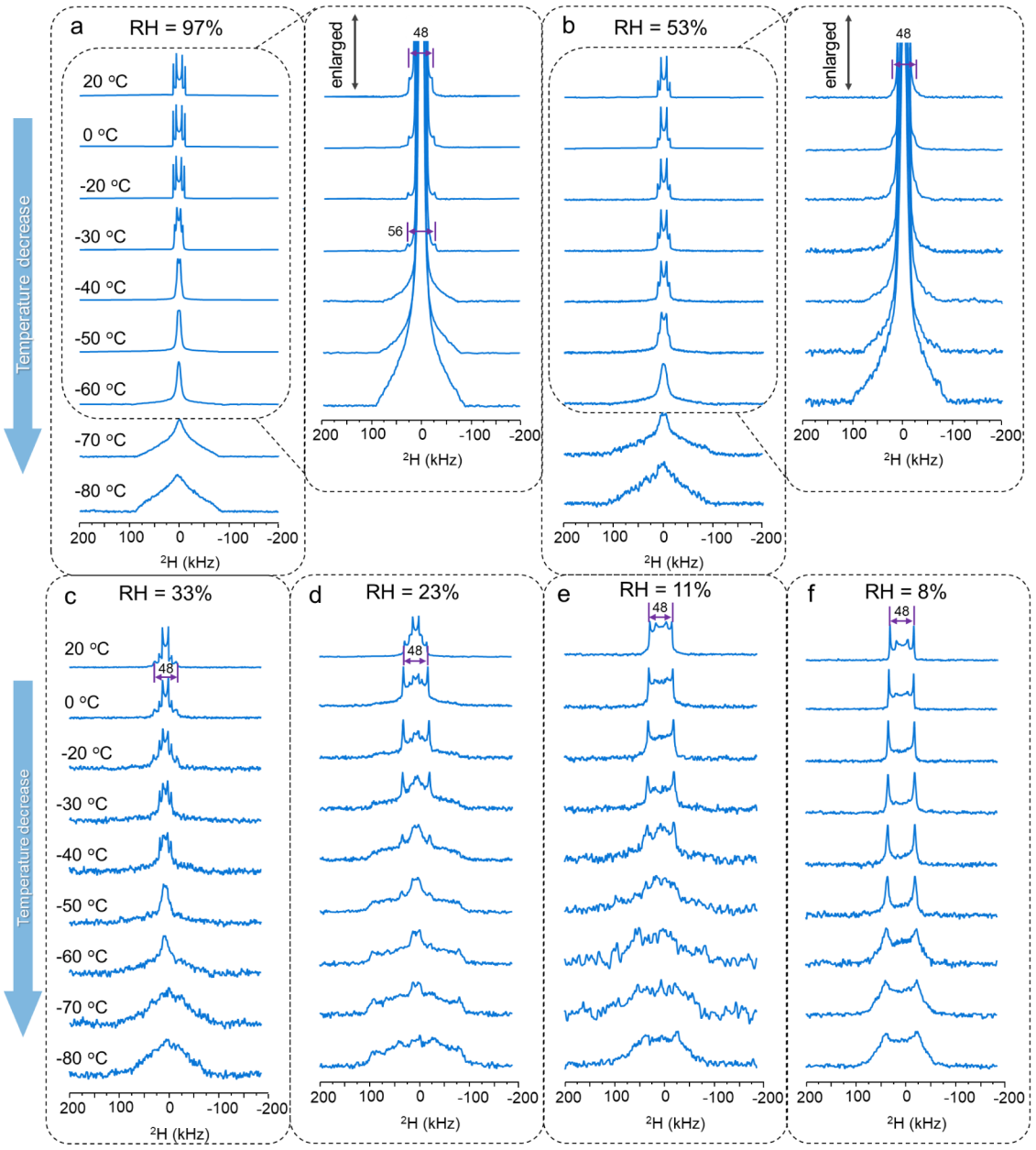

Figure 5. Experimental ^{2}H static VT SSNMR spectra of D_2O adsorbed in Y-BTC under RH values of (a) 97%, (b) 53%, (c) 33%, (d) 23%, (e) 11%, and (f) 8% with decreasing temperatures. Note that the number indicates the line width of doublets in kHz.

aggregating into small water clusters through hydrogen bonding inside the pore channels. This transformation may be triggered by subtle framework changes, such as linker reorientation (*vide infra*),[56] which may create a larger space. The resulting redistribution of water within the structure at high RH upon cooling is schematically illustrated in Scheme 1a. As the temperature further decreases, these clusters undergo a significant reduction in mobility and enter the slow-motion regime, leading to the appearance of a broad, featureless signal that becomes dominant at −70 and −80 °C (Figure 5a). Meanwhile, Type 1 water shows only modest broadening, increasing from 48 kHz at 20 °C to 56 kHz at −30 °C (see enlarged views in Figure 5a). At temperatures below −40 °C, its signal is buried by broadening of the cluster-derived component. The persistence of Type 1 water highlights its strong interaction with Y^{3+} sites, in contrast to the more weakly adsorbed Type 2 and Type 3 species that readily reorganize and become mobile clusters in response to slight linker reorientation within the framework.

To validate the subtle structural changes of the organic linkers that lead to the spectral variations observed in the ^{2}H NMR spectra, VT ^{1}H−^{13}C CP-MAS and ^{1}H MAS NMR spectra were collected for both Y-BTC-act and Y-BTC-act under RH = 97%. In the crystal structure of Y-BTC, there are six crystallographically distinct carbon atoms (C1−C6), as shown in Figure 1a. In both samples, the resonance region between 170 and 176 ppm can be assigned to the two inequivalent carboxyl carbon atoms of BTC linkers, while signals between 131 and 138 ppm correspond to phenyl carbons. For peak assignments in Y-BTC-act (Figure 6a), the ∼2:1 intensity ratio supports the assignment of the 175.9 ppm signal to two equivalent C5 atoms and the 173.0 ppm signal to a single C6 atom. Assigning the six phenyl carbons is more challenging, as the broad envelope peak at around 134.5 ppm is

https://doi.org/10.1021/acs.jpcc.5c05403
J. Phys. Chem. C 2025, 129, 17341−17352

Scheme 1. Schematic Illustration of Water Distribution Upon Cooling under (a) High and (b) Low RH Levels in One Pore Channel[a]

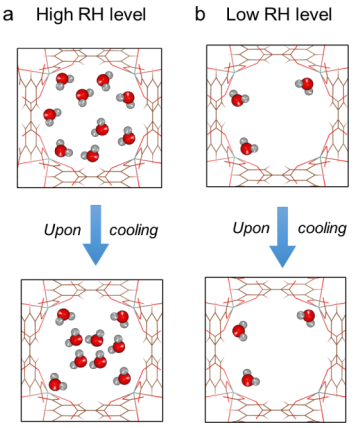

[a]At high RH, where more water molecules are adsorbed in MOF pores, decreasing the temperature induces linker reorientation, promoting the aggregation of water molecules into clusters via hydrogen bonding. At low RH (with fewer adsorbed water molecules), the molecules are insufficient to form clusters at lower temperatures and instead remain strongly adsorbed at open metal sites.

due to the overlap of signals from three quaternary carbons (C2 and C4), which remain unresolved. However, based on the ~2:1 intensity ratio, the other two peaks at 131.5 and 137.9 ppm can be assigned to C3 and C1, respectively. Across the entire temperature range, no peak splitting or significant spectral changes are observed in Y-BTC-act, indicating that in the absence of water, the framework remains rigid and does not undergo significant temperature-induced reorientation of the linkers. In contrast, the ^{13}C spectra of the sample at RH = 97% (Figure 6c) exhibit notable changes upon cooling. At 20 °C, the peaks at 173.6, 170.6, 137.4, and 133.7 ppm are assigned to C5, C6, C1, and C3, respectively. Although slight differences in chemical shifts of carbon environments are observed compared to Y-BTC-act, reflecting linker reorientation upon water removal, the overall assignments remain consistent. Upon cooling to −40 °C, the C5 and C3 atoms become inequivalent, as evidenced by the splitting of 173.6 (C5) and 133.7 (C3) signals into 174.0/173.2 and 134.2/133.3 ppm, respectively. The onset of this splitting occurs within the same temperature range (−20 °C to −60 °C), where the two ^{2}H Pake doublets merge into a single Lorentzian peak in ^{2}H spectra (Figure 5a). This structural evolution is completed at −60 °C and indicates that the linkers adopt different orientations at lower temperatures, producing more inequivalent carbon environments. A similar situation can be found in other MOFs.[57,58] In addition, in situ XRD results (Figure S1b) reveal that upon cooling to approximately −60 °C, the main low-angle diffraction peaks remain stable; however, noticeable differences emerge in the 16−22° and 32−40° regions. These changes suggest subtle structural modifications, such as changes in framework geometry or unit cell parameters, which may weaken water−framework interactions. Such weakening likely promotes the dissociation of adsorbed water, leading to the nucleation of small, bulk-like water clusters.

On the other hand, ^{1}H MAS spectra of Y-BTC-act (Figure 6b) exhibit only one ^{1}H signal, representing equivalent aromatic hydrogen environments in the BTC linkers in the absence of water. In contrast, the spectrum of Y-BTC at an RH of 97% (Figure 6d) shows a dominant sharp peak at 3.9 ppm at 20 °C, attributed to adsorbed water. The presence of a single water signal suggests that, although water molecules occupy different adsorption positions, they may share similar isotropic chemical shift values (δ_{iso}) or experience fast exchange between different positions on the NMR time scale.[59] In addition, a small peak at 8.7 ppm with a shoulder at 9.4 ppm corresponds to the aromatic protons (H1 and H2) of the BTC linkers (Figure 1a).[60] As temperature decreases, the water resonance shifts from 3.9 to 4.5 ppm and becomes much broader. This 4.5 ppm signal is characteristic of bulk-like water engaged in extensive hydrogen bonding,[61] providing evidence for the formation of water clusters at lower temperatures (as illustrated in Scheme 1a). Moreover, the accompanying signal broadening reflects reduced water mobility and thus increased dipolar interactions at lower temperatures. After returning to 20 °C, both the ^{1}H−^{13}C CP-MAS and ^{1}H MAS NMR spectra are nearly identical to those measured before cooling (Figure S6), demonstrating that the conversion between bulk-like water clusters and adsorbed water in Y-BTC under an RH of 97% is reversible. This observation supports that upon returning to 20 °C, water molecules are readsorbed at specific positions, and the structure reverts to the original configuration.

A similar trend in the chemical shift of the water signal in ^{1}H MAS spectra is also observed across the entire range of RH levels (Figure S7). At RH = 8%, the water signal is considerably broader and more shielded, appearing at 3.0 ppm, and it gradually shifts to 3.9 ppm as RH increases to 97%. This shift is indicative of more extensive hydrogen bonding at higher RH levels. Conversely, the more shielded and broadened signal at low RH suggests stronger interactions between water and the MOF framework, likely due to preferential adsorption at open metal sites. Additionally, the relative intensity of the water signal compared to that of the aromatic protons increases with RH, reflecting the greater water uptake at higher RH levels.

The findings presented above are in excellent agreement with ^{2}H SSNMR results (Figure 5). At RH = 97%, 53%, and 33% (Figure 5a−c), all spectra exhibit similar Lorentzian broadening upon cooling, indicative of the formation of hydrogen-bonded water clusters. In contrast, at RH = 11% and 8% (Figure 5e,f), no obvious Lorentzian features are observed. Instead, the spectra retain the Type 1 water signal, which is associated with strongly adsorbed water at the open metal sites. This may imply that at such low RH levels, the water content is insufficient to form hydrogen-bonded water clusters. Consequently, water molecules remain bound to the open metal sites with restricted mobility, giving rise to broadened lines at low temperatures. The corresponding spatial distribution of water under the low-RH condition is illustrated in Scheme 1b. Furthermore, the sample at RH = 23% (Figure 5d) can be considered an intermediate state, exhibiting partial features of both adsorption modes, bridging the behavior between the low- and high-RH conditions.

Heating the samples from room temperature to 100 °C across different RH levels provides additional insight into the water dynamics. As shown in the ^{2}H SSNMR spectra (Figure 7), a consistent trend is the narrowing of the Type 1 water signal from 20 to 100 °C, indicating enhanced molecular mobility at open metal sites. At lower RH levels (RH ≤23%),

https://doi.org/10.1021/acs.jpcc.5c05403
J. Phys. Chem. C 2025, 129, 17341−17352

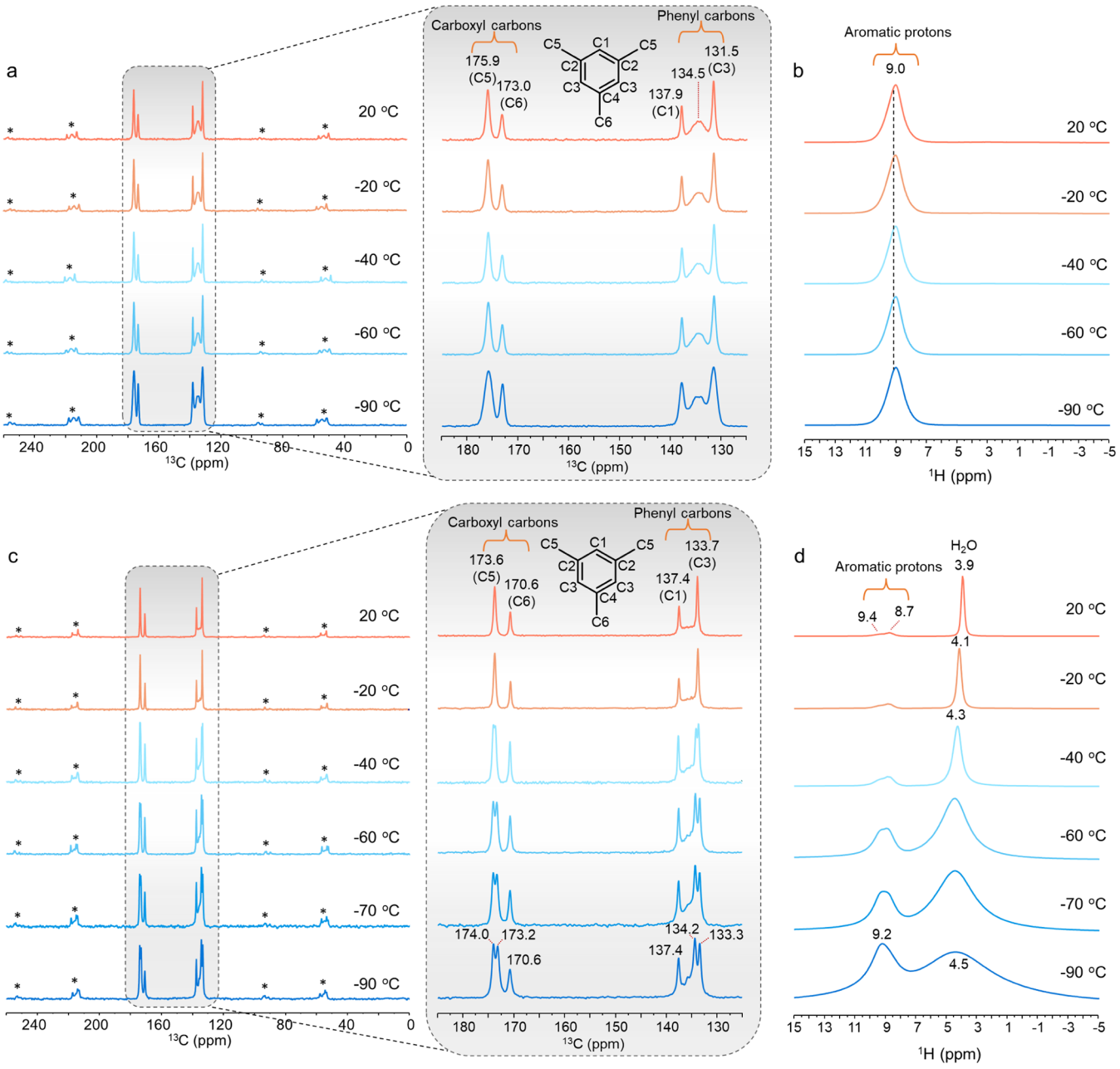

Figure 6. (a) $^{1}H-^{13}C$ CP-MAS and (b) ^{1}H MAS VT SSNMR spectra of Y-BTC-act. (c) $^{1}H-^{13}C$ CP-MAS and (d) ^{1}H MAS VT SSNMR spectra of Y-BTC under an RH of 97%. CP-MAS spectra are obtained with a contact time of 3 ms and a recycle delay of 5 s. All the spectra are acquired at a spinning rate of 8 kHz. Asterisk represents the spinning sidebands.

increasing temperature not only boosts water mobility but also drives a redistribution of water molecules from the open metal sites (Type 1) to less strongly adsorbed environments (Types 2 and 3). For instance, at RH = 23%, the spectrum at 20 °C is dominated by Type 1 water; however, upon heating, the intensities of Type 2 and 3 signals increase and eventually surpass that of Type 1, suggesting partial desorption and migration of water into positions with greater motional freedom. In contrast, this thermally induced redistribution is less discernible at higher RH levels (e.g., 53% and 97%) due to the already dominant presence of Type 2 and Type 3 water, as reflected in their higher relative intensities. Nevertheless, the Type 1 signal remains detectable, though only upon magnification, confirming that a fraction of water molecules remain coordinated to the open metal sites even at elevated temperatures.

CONCLUSION

In conclusion, this study provides a comprehensive investigation of water adsorption behavior and dynamics in Y-BTC through a combination of XAFS, SSNMR, and Monte Carlo simulations. First, in situ XAFS confirms that the removal of coordinated water from Y^{3+} sites reduces the coordination number from 7 to 6, generating open metal sites and inducing subtle changes in the local bonding environment. This dehydration is further supported by the downfield shift of the ^{89}Y NMR signal, consistent with a lower coordination number.

https://doi.org/10.1021/acs.jpcc.5c05403
J. Phys. Chem. C 2025, 129, 17341−17352

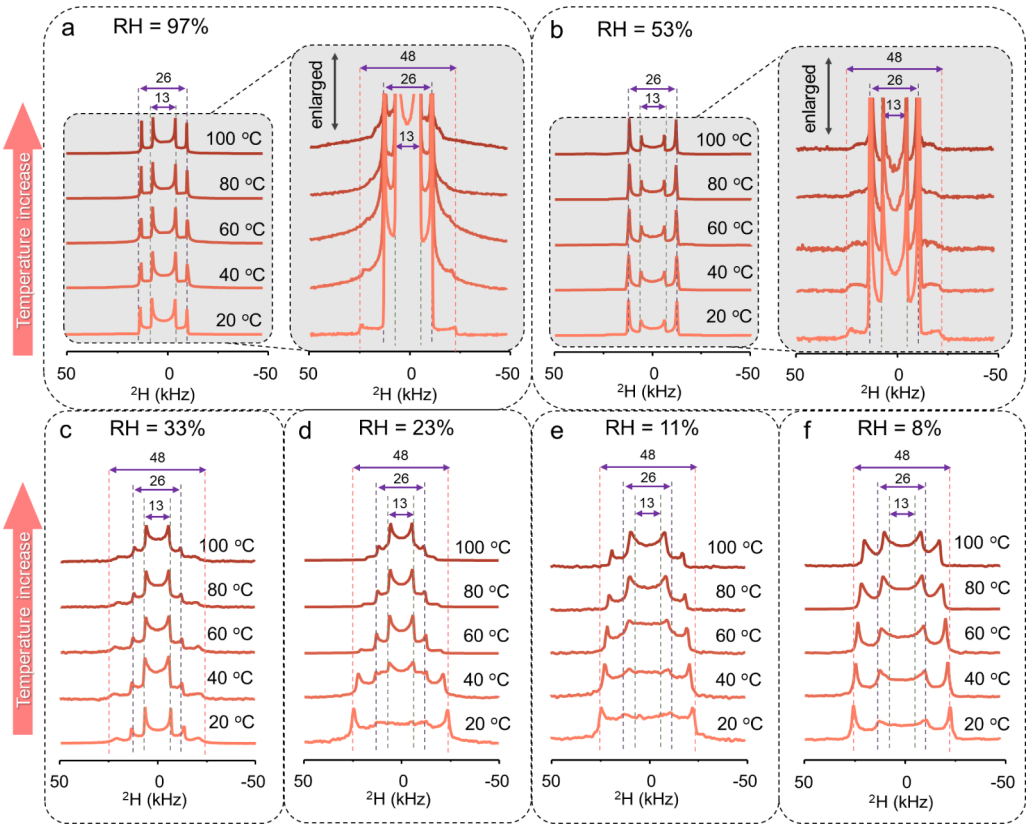

Figure 7. Experimental ^{2}H static VT SSNMR spectra of D_2O adsorbed in Y-BTC under RH values of (a) 97%, (b) 53%, (c) 33%, (d) 23%, (e) 11%, and (f) 8% with increasing temperatures. Note that the number indicates the line width of doublets in kHz.

Second, ^{2}H SSNMR spectra under varying RH conditions uncover three distinct types of adsorbed water, characterized by different mobilities and local environments: strongly bound water at open metal sites (Type 1), water interacting with BTC linkers (Type 2), and more mobile water forming hydrogen-bonded clusters within the pore channels (Type 3). At low RH, the spectra are dominated by Type 1 water, exhibiting the broadest Pake doublets due to restricted motion, accompanied by Type 2 water, showing a narrower Pake pattern at room temperature. As RH increases, Type 3 water appears with the narrowest Pake pattern. These spectral assignments are corroborated by MC simulations.

Finally, VT ^{2}H SSNMR reveals that both cooling and heating the samples can redistribute water among different positions. Upon cooling, subtle structural changes may weaken water-framework interactions, facilitating the aggregation of adsorbed water into small hydrogen-bonded clusters. Upon heating, water initially coordinated at open metal sites partially relocates to less constrained environments, suggesting that the water–framework interactions are relatively weak to allow facile desorption and redistribution. This dynamic behavior offers a deeper understanding of water–framework interactions, which is crucial for the rational design of MOFs for water-based applications.

■ ASSOCIATED CONTENT

Supporting Information

The Supporting Information is available free of charge at https://pubs.acs.org/doi/10.1021/acs.jpcc.5c05403.

Experimental details and additional characterization (XRD, TGA, water vapor adsorption isotherm, XANES, NMR data, and EXAFS fitting) (PDF)

■ AUTHOR INFORMATION

Corresponding Authors

Jun Zhong − *Institute of Functional Nano and Soft Materials Laboratory (FUNSOM), Jiangsu Key Laboratory for Carbon-Based Functional Materials & Devices, Soochow University, Suzhou 215123, China;* orcid.org/0000-0002-8768-1843; Email: jzhong@suda.edu.cn

Tsun-Kong Sham − *Department of Chemistry, The University of Western Ontario, London, Ontario N6A 5B7, Canada;* orcid.org/0000-0003-1928-6697; Email: tsham@uwo.ca

Yining Huang − *Department of Chemistry, The University of Western Ontario, London, Ontario N6A 5B7, Canada;* orcid.org/0000-0001-9265-5896; Email: yhuang@uwo.ca

Authors

Jiabin Xu − *Department of Chemistry, The University of Western Ontario, London, Ontario N6A 5B7, Canada; Institute of Functional Nano and Soft Materials Laboratory (FUNSOM), Jiangsu Key Laboratory for Carbon-Based Functional Materials & Devices, Soochow University, Suzhou 215123, China;* orcid.org/0000-0002-9693-2261

Jingsong Wang − *Department of Chemistry, The University of Western Ontario, London, Ontario N6A 5B7, Canada*

Xinyue Sheng − *Center for Rare Earth and Inorganic Functional Materials, Tianjin Key Lab for Rare Earth Materials and Applications, School of Materials Science and*

https://doi.org/10.1021/acs.jpcc.5c05403
J. Phys. Chem. C 2025, 129, 17341−17352

Engineering & National Institute for Advanced Materials, Nankai University, Tianjin 300350, P.R. China; orcid.org/0009-0009-7298-8824

Hui Ding − *Center for Rare Earth and Inorganic Functional Materials, Tianjin Key Lab for Rare Earth Materials and Applications, School of Materials Science and Engineering & National Institute for Advanced Materials, Nankai University, Tianjin 300350, P.R. China*

Jun Xu − *Center for Rare Earth and Inorganic Functional Materials, Tianjin Key Lab for Rare Earth Materials and Applications, School of Materials Science and Engineering & National Institute for Advanced Materials, Nankai University, Tianjin 300350, P.R. China;* orcid.org/0000-0003-3507-0159

Shoushun Chen − *Frontiers Science Center for Rare Isotopes, Lanzhou Magnetic Resonance Center, College of Chemistry and Chemical Engineering, Lanzhou University, Lanzhou 730000, China;* orcid.org/0009-0009-4315-015X

Ivan Hung − *National High Magnetic Field Laboratory, Tallahassee, Florida 32310, United States;* orcid.org/0000-0001-8916-739X

Zhehong Gan − *National High Magnetic Field Laboratory, Tallahassee, Florida 32310, United States;* orcid.org/0000-0002-9855-5113

Youyong Li − *Institute of Functional Nano and Soft Materials Laboratory (FUNSOM), Jiangsu Key Laboratory for Carbon-Based Functional Materials & Devices, Soochow University, Suzhou 215123, China;* orcid.org/0000-0002-5248-2756

Complete contact information is available at: https://pubs.acs.org/10.1021/acs.jpcc.5c05403

Notes

The authors declare no competing financial interest.

■ ACKNOWLEDGMENTS

The authors acknowledge Mathew Willans of the J.B. Stothers NMR Facility at Western University for the SSNMR experiments. The authors also thank Ning Chen and Weifeng Chen at HXMA of CLS for their assistance in in situ XAFS experiments. Y.H. thanks the Natural Science and Engineering Research Council (NSERC) of Canada for a Discovery Grant. J.X. thanks the financial support from the National Natural Science Foundation of China (22471128). The National High Magnetic Field Laboratory is supported by the National Science Foundation through NSF/DMR-2128556 and the State of Florida. The magnet and NMR instrumentation were supported by the NSF (DMR-1039938 and DMR-0603042) and NIH (BTRR 1P41GM122698 and RM1GM148766). T.S. also thanks the Canada Research Chair (CRC), Canada Foundation for Innovation (CFI), and the University of Western Ontario. The Canadian Light Source is supported by CFI, NSERC, the National Research Council (NRC), the Canadian Institutes of Health Research (CIHR), the Government of Saskatchewan, and the University of Saskatchewan.

■ REFERENCES

(1) Lu, H.; Shi, W.; Guo, Y.; Guan, W.; Lei, C.; Yu, G. Materials Engineering for Atmospheric Water Harvesting: Progress and Perspectives. *Adv. Mater.* **2022**, *34* (12), 2110079.

(2) Jarimi, H.; Powell, R.; Riffat, S. Review of sustainable methods for atmospheric water harvesting. *Int. J. Low-Carbon Technol.* **2020**, *15*, 253−276.

(3) Zhou, X.; Lu, H.; Zhao, F.; Yu, G. Atmospheric Water Harvesting: A Review of Material and Structural Designs. *ACS Mater. Lett.* **2020**, *2*, 671−684.

(4) Cui, S.; Qin, M.; Marandi, A.; Steggles, V.; Wang, S.; Feng, X.; Nouar, F.; Serre, C. Metal-Organic Frameworks as advanced moisture sorbents for energy-efficient high temperature cooling. *Sci. Rep.* **2018**, *8* (1), 15284.

(5) Lin, L.; Ge, Y.; Zhang, H.; Wang, M.; Xiao, D.; Ma, D. Heterogeneous Catalysis in Water. *JACS Au* **2021**, *1*, 1834−1848.

(6) Chang, C.-R.; Huang, Z.-Q.; Li, J. The promotional role of water in heterogeneous catalysis: mechanism insights from computational modeling. *Wiley Interdiscip. Rev.: Comput. Mol. Sci.* **2016**, *6*, 679−693.

(7) Zhang, B.; Zheng, Y.; Ma, T.; Yang, C.; Peng, Y.; Zhou, Z.; Zhou, M.; Li, S.; Wang, Y.; Cheng, C. Designing MOF Nanoarchitectures for Electrochemical Water Splitting. *Adv. Mater.* **2021**, *33* (17), 2006042.

(8) Li, X.; Hao, X.; Abudula, A.; Guan, G. Nanostructured catalysts for electrochemical water splitting: current state and prospects. *J. Mater. Chem. A* **2016**, *4*, 11973−12000.

(9) Hata, K.; Futaba, D. N.; Mizuno, K.; Namai, T.; Yumura, M.; Iijima, S. Water-assisted highly efficient synthesis of impurity-free single-walled carbon nanotubes. *Science* **2004**, *306*, 1362−1364.

(10) Karthaus, O.; Maruyama, N.; Cieren, X.; Shimomura, M.; Hasegawa, H.; Hashimoto, T. Water-assisted formation of micrometer-size honeycomb patterns of polymers. *Langmuir* **2000**, *16*, 6071−6076.

(11) Zhang, X.; Bai, X.; Wu, H.; Zhang, X.; Sun, C.; Zhang, Y.; Zhang, W.; Zheng, W.; Yu, W. W.; Rogach, A. L. Water-assisted size and shape control of CsPbBr3 perovskite nanocrystals. *Angew. Chem., Int. Ed.* **2018**, *57*, 3337−3342.

(12) Hanikel, N.; Prévot, M. S.; Yaghi, O. M. MOF water harvesters. *Nat. Nanotechnol.* **2020**, *15*, 348−355.

(13) Canivet, J.; Fateeva, A.; Guo, Y.; Coasne, B.; Farrusseng, D. Water adsorption in MOFs: fundamentals and applications. *Chem. Soc. Rev.* **2014**, *43*, 5594−5617.

(14) Hall, J. N.; Bollini, P. Quantification of Open-Metal Sites in Metal−Organic Frameworks Using Irreversible Water Adsorption. *Langmuir* **2020**, *36*, 1345−1356.

(15) Rieth, A. J.; Hunter, K. M.; Dincă, M.; Paesani, F. Hydrogen bonding structure of confined water templated by a metal-organic framework with open metal sites. *Nat. Commun.* **2019**, *10* (1), 4771.

(16) Auckett, J. E.; Ogilvie, S. H.; Duyker, S. G.; Southon, P. D.; Kepert, C. J.; Peterson, V. K. Flexible Yttrium Coordination Geometry Inhibits "Bare-Metal" Guest Interactions in the Metal-Organic Framework Y(btc). *Energies* **2016**, *9*, 836.

(17) Weigler, M.; Brodrecht, M.; Breitzke, H.; Dietrich, F.; Sattig, M.; Buntkowsky, G.; Vogel, M. ^{2}H NMR Studies on Water Dynamics in Functionalized Mesoporous Silica. *Z. Phys. Chem.* **2018**, *232*, 1041−1058.

(18) Sahu, K.; Mondal, S. K.; Ghosh, S.; Bhattacharyya, K. Ultrafast Dynamics in Biological Systems and in Nano-Confined Environments. *Bull. Chem. Soc. Jpn.* **2007**, *80*, 1033−1043.

(19) Rasaiah, J. C.; Garde, S.; Hummer, G. Water in Nonpolar Confinement: From Nanotubes to Proteins and Beyond*. *Annu. Rev. Phys. Chem.* **2008**, *59*, 713−740.

(20) Saraci, F.; Quezada-Novoa, V.; Donnarumma, P. R.; Howarth, A. J. Rare-earth metal−organic frameworks: from structure to applications. *Chem. Soc. Rev.* **2020**, *49*, 7949−7977.

(21) Younis, S. A.; Bhardwaj, N.; Bhardwaj, S. K.; Kim, K.-H.; Deep, A. Rare earth metal−organic frameworks (RE-MOFs): Synthesis, properties, and biomedical applications. *Coord. Chem. Rev.* **2021**, *429*, 213620.

(22) Jiang, H.-L.; Tsumori, N.; Xu, Q. A series of (6,6)-connected porous lanthanide-organic framework enantiomers with high thermostability and exposed metal sites: scalable syntheses, structures, and sorption properties. *Inorg. Chem.* **2010**, *49*, 10001.

(23) Li, Z.; Ma, S.; Chen, C.; Qu, G.; Jin, W.; Zhao, Y. Efficient capture of arsenate from alkaline smelting wastewater by acetate

modulated yttrium based metal-organic frameworks. *Chem. Eng. J.* **2020**, *397*, 125292.
(24) Luo, J.; Xu, H.; Liu, Y.; Zhao, Y.; Daemen, L. L.; Brown, C.; Timofeeva, T. V.; Ma, S.; Zhou, H.-C. Hydrogen Adsorption in a Highly Stable Porous Rare-Earth Metal-Organic Framework: Sorption Properties and Neutron Diffraction Studies. *J. Am. Chem. Soc.* **2008**, *130*, 9626−9627.
(25) Kökçam-Demir, Ü.; Goldman, A.; Esrafili, L.; Gharib, M.; Morsali, A.; Weingart, O.; Janiak, C. Coordinatively unsaturated metal sites (open metal sites) in metal−organic frameworks: design and applications. *Chem. Soc. Rev.* **2020**, *49*, 2751−2798.
(26) Britt, D.; Furukawa, H.; Wang, B.; Glover, T. G.; Yaghi, O. M. Highly efficient separation of carbon dioxide by a metal-organic framework replete with open metal sites. *ProcNatl. Acad. Sci. U. S. A.* **2009**, *106*, 20637−20640.
(27) Kong, X.; Scott, E.; Ding, W.; Mason, J. A.; Long, J. R.; Reimer, J. A. CO_2 Dynamics in a Metal−Organic Framework with Open Metal Sites. *J. Am. Chem. Soc.* **2012**, *134*, 14341−14344.
(28) Ogilvie, S. H.; Duyker, S. G.; Southon, P. D.; Peterson, V. K.; Kepert, C. J. Host−guest adsorption behavior of deuterated methane and molecular oxygen in a porous rare-earth metal−organic framework. *Powder Diffr.* **2014**, *29*, S96−S101.
(29) Xu, J.; Zhang, W.; Liu, J.; Zhong, J.; Sham, T.-K.; Huang, Y. CO_2 Dynamics in a Flexible Metal-Organic Framework with Gate-Opening Phenomenon. *Chem. Eur. J.* **2024**, *30* (71), No. e202402775.
(30) Zeng, H.; Xie, M.; Huang, Y. L.; Zhao, Y.; Xie, X. J.; Bai, J. P.; Wan, M. Y.; Krishna, R.; Lu, W.; Li, D. Induced fit of C_2H_2 in a flexible MOF through cooperative action of open metal sites. *Angew. Chem., Int. Ed.* **2019**, *58*, 8515−8519.
(31) Kim, Y.; Haldar, R.; Kim, H.; Koo, J.; Kim, K. The guest-dependent thermal response of the flexible MOF $Zn_2(BDC)_2(DABCO)$. *Dalton Trans.* **2016**, *45*, 4187−4192.
(32) Antonijevic, S.; Wimperis, S. Refocussing of chemical and paramagnetic shift anisotropies in ^{2}H NMR using the quadrupolar-echo experiment. *J. Magn. Reson.* **2003**, *164*, 343−350.
(33) Massiot, D.; Fayon, F.; Capron, M.; King, I.; Le Calvé, S.; Alonso, B.; Durand, J.-O.; Bujoli, B.; Gan, Z.; Hoatson, G. Modelling one- and two-dimensional solid-state NMR spectra. *Magn. Reson. Chem.* **2002**, *40*, 70−76.
(34) Chandran, C. V.; Schreuders, H.; Dam, B.; Janssen, J. W. G.; Bart, J.; Kentgens, A. P. M.; van Bentum, P. J. M. Solid-State NMR Studies of the Photochromic Effects of Thin Films of Oxygen-Containing Yttrium Hydride. *J. Phys. Chem. C* **2014**, *118*, 22935−22942.
(35) Ravel, B.; Newville, M. ATHENA , ARTEMIS , HEPHAESTUS: data analysis for X-ray absorption spectroscopy using IFEFFIT. *J. Synchrotron Rad.* **2005**, *12* (4), 537−541.
(36) Macedonia, M. D.; Maginn, E. J. A biased grand canonical Monte Carlo method for simulating adsorption using all-atom and branched united atom models. *Mol. Phys.* **1999**, *96*, 1375−1390.
(37) Vreven, T.; Frisch, M. J.; Kudin, K. N.; Schlegel, H. B.; Morokuma, K. Geometry optimization with QM/MM methods II: Explicit quadratic coupling. *Mol. Phys.* **2006**, *104*, 701−714.
(38) Vreven, T.; Byun, K. S.; Komáromi, I.; Dapprich, S.; Montgomery, J. A., Jr.; Morokuma, K.; Frisch, M. J. Combining Quantum Mechanics Methods with Molecular Mechanics Methods in ONIOM. *J. Chem. Theory Comput.* **2006**, *2* (3), 815−826.
(39) Zhang, S.; Zhao, S.; Xia, M.; Zhang, E.; Zuo, X.; Xu, T. Optimum diameter of single-walled carbon nanotubes in carbon nanotube ropes. *Phys. Rev. B* **2004**, *70*, 035403.
(40) Zhou, X. W.; Johnson, R. A.; Wadley, H. N. G. Misfit-energy-increasing dislocations in vapor-deposited CoFe/NiFe multilayers. *Phys. Rev. B* **2004**, *69*, 144113.
(41) Yamamoto, T. Assignment of pre-edge peaks in K-edge x-ray absorption spectra of 3d transition metal compounds: electric dipole or quadrupole? *x-Ray Spectrom.* **2008**, *37*, 572−584.
(42) Muñoz, M.; Argoul, P.; Farges, F. Continuous Cauchy wavelet transform analyses of EXAFS spectra: A qualitative approach. *Am. Mineral.* **2003**, *88*, 694−700.
(43) Kawata, K.; Maekawa, H.; Nemoto, T.; Yamamura, T. Local structure analysis of YSZ by Y-89 MAS-NMR. *Solid State Ionics* **2006**, *177*, 1687−1690.
(44) Wu, J.; Boyle, T. J.; Shreeve, J. L.; Ziller, J. W.; Evans, W. J. CP/MAS yttrium-89 NMR spectroscopy: a facile method for characterizing yttrium-containing solids. *Inorg. Chem.* **1993**, *32*, 1130−1134.
(45) Xu, J.; Jiang, S.; Du, Y. Unravelling the Mystery of Solid Solutions: A Case Study of ^{89}Y Solid-State NMR Spectroscopy. *ChemPhyschem* **2020**, *21*, 825−836.
(46) Liu, Z.; Liang, L.; Xiao, D.; Ji, Y.; Zhao, Z.; Xu, J.; Hou, G. ^{89}Y chemical shift anisotropy: a sensitive structural probe of layered yttrium hydroxides revealed by solid-state NMR spectroscopy and DFT calculations. *Phys. Chem. Chem. Phys.* **2021**, *23*, 27244−27252.
(47) Smith, M. E. Recent progress in solid-state NMR of low-γ nuclei. In *Annual Reports on NMR Spectroscopy*; Academic Press, 2001; Vol. *43*, pp. 121−175.
(48) Harazono, T.; Watanabe, T. Chemical Shift, Chemical Shift Anisotropy, and Spin-Lattice Relaxation Time in ^{89}Y-MAS and -Static NMR of Yttrium Compounds. *Bull. Chem. Soc. Jpn.* **1997**, *70*, 2383−2388.
(49) Merwin, L. H.; Sebald, A. The first 89Y CP-MAS spectra. *J. Magn. Reson. (1969)* **1990**, *88*, 167−171.
(50) Kim, N.; Stebbins, J. F. Vacancy and Cation Distribution in Yttria-Doped Ceria: An ^{89}Y and ^{17}O MAS NMR Study. *Chem. Mater.* **2007**, *19*, 5742−5747.
(51) Feng, Z.; Xiao, D.; Liu, Z.; Hou, G.; Xu, J. "X Factor" in the Structure and Anion Exchange of Layered Yttrium Hydroxides. *J. Phys. Chem. C* **2021**, *125*, 7251−7258.
(52) Greenspan, L. Humidity fixed points of binary saturated aqueous solutions. *J. Res. Natl. Bur. Stand. A Phys. Chem.* **1977**, *81A* (1), 89−96.
(53) Omichi, H.; Ueda, T.; Miyakubo, K.; Eguchi, T. Solid-state ^{2}H NMR Study of Nanocrystal Formation of D_2O and Their Dynamic Aspects in ACF Hydrophobic Nanospaces. *Chem. Lett.* **2007**, *36*, 256−257.
(54) Steinrücken, E.; Wissel, T.; Brodrecht, M.; Breitzke, H.; Regentin, J.; Buntkowsky, G.; Vogel, M. ^{2}H NMR study on temperature-dependent water dynamics in amino-acid functionalized silica nanopores. *J. Chem. Phys.* **2021**, *154* (11), 114702.
(55) Birsa Čelič, T.; Mazaj, M.; Guillou, N.; Elkaïm, E.; El Roz, M.; Thibault-Starzyk, F.; Mali, G.; Rangus, M.; Čendak, T.; Kaučič, V.; et al. Study of Hydrothermal Stability and Water Sorption Characteristics of 3-Dimensional Zn-Based Trimesate. *J. Phys. Chem. C* **2013**, *117*, 14608−14617.
(56) Xu, J.; Sinelnikov, R.; Huang, Y. Capturing Guest Dynamics in Metal-Organic Framework CPO-27-M (M = Mg, Zn) by ^{2}H Solid-State NMR Spectroscopy. *Langmuir* **2016**, *32*, 5468.
(57) Chen, S.; Lucier, B. E. G.; Boyle, P. D.; Huang, Y. Understanding The Fascinating Origins of CO_2 Adsorption and Dynamics in MOFs. *Chem. Mater.* **2016**, *28*, 5829−5846.
(58) Mukherjee, S.; Chen, S.; Bezrukov, A. A.; Mostrom, M.; Terskikh, V. V.; Franz, D.; Wang, S.-Q.; Kumar, A.; Chen, M.; Space, B.; et al. Ultramicropore Engineering by Dehydration to Enable Molecular Sieving of H_2 by Calcium Trimesate. *Angew. Chem., Int. Ed.* **2020**, *59*, 16188−16194.
(59) Bain, A. D. Chemical exchange in NMR. *Prog. Nucl. Magn. Reson. Spectrosc.* **2003**, *43*, 63−103.
(60) Mali, G.; Trebosc, J.; Martineau, C.; Mazaj, M. Structural Study of Mg-Based Metal−Organic Frameworks by X-ray Diffraction, ^{1}H, ^{13}C, and ^{25}Mg Solid-State NMR Spectroscopy, and First-Principles Calculations. *J. Phys. Chem. C* **2015**, *119*, 7831−7841.
(61) Venel, F.; Volkringer, C.; Lafon, O.; Pourpoint, F. Probing adsorption of water and DMF in UiO-66(Zr) using solid-state NMR. *Solid State Nucl. Magn. Reson.* **2022**, *120*, 101797.